to Neptune, whereas the second-largest moons (like Caliban or S/2000 S 3) would have magnitudes of 24–25. Thus if a similar irregular system is present around Neptune, its smaller members were beyond the limits of the deepest known survey[3] and Nereid (Neptune's only distant satellite) is only the brightest member of a population waiting patiently to be discovered. □

Received 15 February; accepted 9 May 2001.

1. Peale, S. J. Origin and evolution of the natural satellites. *Annu. Rev. Astron. Astrophys.* **37,** 533–602 (1999).
2. Gladman, B. J. *et al.* Discovery of two distant irregular moons of Uranus. *Nature* **392,** 897–899 (1998).
3. Gladman, B. J. *et al.* The discovery of Uranus XIX, XX, and XXI. *Icarus* **147,** 320–324 (2000); erratum **148,** 320 (2000).
4. Marsden, B. G. S/1999 J 1. *IAU Circ.* **7460** (2000).
5. Marsden, B. G. S/1975 J 1 = S/2000 J 1. *IAU Circ.* **7640** (2000).
6. Green, D. Satellites of Jupiter. *IAU Circ.* **7555** (2001).
7. Pollack, J. B., Burns, J. A. & Tauber, M. E. Gas drag in primordial circumplanetary envelopes: A mechanism for satellite capture. *Icarus* **37,** 587–611 (1979).
8. Colombo, G. & Franklin, F. A. On the formation of the outer satellite groups of Jupiter. *Icarus* **30,** 186–189 (1971).
9. Heppenheimer, T. A. & Porco, C. C. New contributions to the problem of capture. *Icarus* **30,** 385–401 (1977).
10. Saha, P. & Tremaine, S. The orbits of the retrograde jovian satellites. *Icarus* **106,** 549–562 (1993).
11. Hénon, M. Numerical exploration of the restricted problem. VI. Hill's case: Non-periodic orbits. *Astron. Astrophys.* **9,** 24–36 (1970).
12. Hamilton, D. P. & Burns, J. A. Orbital stability zones about asteroids. *Icarus* **92,** 118–131 (1991).
13. Hamilton, D. P. & Krivov, A. V. Dynamics of distant moons of asteroids. *Icarus* **128,** 241–249 (1997).
14. Wiegert, P., Innanen, K. & Mikkola, S. The stability of quasi satellites in the outer solar system. *Astron. J.* **119,** 1978–1984 (2000).
15. Kozai, Y. Secular perturbations of asteroids with high inclination and eccentricity. *Astron. J.* **67,** 591–598 (1962).
16. Kinoshita, H. & Nakai, H. Secular perturbations of fictitious satellites of Uranus. *Celest. Mech.* **52,** 293–303 (1991).
17. Clark, R. N., Fanale, F. P. & Gaffey, M. J. in *Satellites* (eds Burns, J. A. & Matthews, M. S.) 437–492 (Univ. Arizona Press, Tucson, 1986).
18. Luu, J. CCD photometry and spectroscopy of the outer jovian satellites. *Astron. J.* **102,** 1213–1225 (1991).
19. Jarvis, K. S. *et al.* JVI Himalia: New compositional evidence and interpretations for the origin of Jupiter's small satellites. *Icarus* **145,** 445–453 (2000).
20. Farinella, P. *et al.* The injection of asteroid fragments into resonances. *Icarus* **101,** 174–187 (1993).
21. Smith, B. A. *et al.* A new look at the Saturn system. *Science* **215,** 504–537 (1982).
22. Colwell, J. E. & Esposito, L. W. Origins of the rings of Uranus and Neptune. II. Initial distributions of disrupted satellite fragments. *J. Geophys. Res.* **98,** 7387–7401 (1993).
23. Porco, C. C. *et al.* in *Neptune and Triton* (ed. Cruikshank, D. P.) 703–804 (Univ. Arizona Press, Tucson, 1995).
24. Tanga, P. *et al.* On the size distribution of asteroid families: The role of geometry. *Icarus* **141,** 65–78 (1999).
25. Thomas, P. *et al.* Phoebe: Voyager 2 observations. *J. Geophys. Res.* **88,** 8736–8742 (1986).
26. Simonelli, D. *et al.* Phoebe: Albedo map and photometric properties. *Icarus* **138,** 249–258 (1999).
27. Gladman, B. *et al.* Pencil-beam surveys for faint trans-neptunian comets. *Astron. J.* **116,** 2042–2054 (1998).
28. McKinnon, W., Lunine, J. I. & Banfield, D. in *Neptune and Triton* (ed. Cruikshank, D. P.) 807–878 (Univ. Arizona Press, Tucson, 1995).
29. Marsden, B. G. S/2000 S 1 and S/2000 S 2. *IAU Circ.* **7512** (2000).
30. Marsden, B. G. S/2000 S 3 and S/2000 S 4. *IAU Circ.* **7513** (2000).
31. Marsden, B. G. S/2000 S 5 and S/2000 S 6. *IAU Circ.* **7521** (2000).
32. Marsden, B. G. S/2000 S 7, S/2000 S 8 and S/2000 S9. *IAU Circ.* **7538** (2000).
33. Marsden, B. G. S/2000 S 10. *IAU Circ.* **7539** (2000).
34. Green, D. S/2000 S 11. *IAU Circ.* **7545** (2000).
35. Green, D. S/2000 S 12. *IAU Circ.* **7548** (2000).

Acknowledgements

The Canada–France–Hawaii telescope is operated by the National Research Council of Canada, le Centre National de la Recherche Scientifique de France, and the University of Hawaii. Observations for the ESO 2.2-m telescope and the VLT were collected at the European Southern Observatory, Chile. Observations at the Palomar Observatory were made as part of a continuing collaborative agreement between the California Institute of Technology and Cornell University. Kitt Peak National Observatory, part of the National Optical Astronomy Observatories, is operated by the Association of Universities for Research in Astronomy, Inc. (AURA) under cooperative agreement with the National Science Foundation. The Nordic Optical Telescope is operated on the island of La Palma jointly by Denmark, Finland, Iceland, Norway and Sweden, in the Spanish Observatorio del Roque de los Muchachos of the Instituto de Astrofisica de Canarias. We gratefully acknowledge financing from the French Research Ministry ACI Jeunes Chercheurs programme, the Institut National de Science de l'Univers, from the European Southern Observatory, from the NASA Planetary Astronomy programme and the Natural Sciences and Engineering Research Council of Canada.

Correspondence and requests for materials should be addressed to B.G. (e-mail: gladman@obs-nice.fr).

Ion-beam sculpting at nanometre length scales

Jiali Li*, Derek Stein†, Ciaran McMullan‡, Daniel Branton‡, Michael J. Aziz† & Jene A. Golovchenko*†

** Department of Physics, † Division of Engineering and Applied Sciences, and ‡ Department of Molecular and Cellular Biology, Harvard University, Cambridge, Massachusetts 02138, USA*

Manipulating matter at the nanometre scale is important for many electronic, chemical and biological advances[1–3], but present solid-state fabrication methods do not reproducibly achieve dimensional control at the nanometre scale. Here we report a means of fashioning matter at these dimensions that uses low-energy ion beams and reveals surprising atomic transport phenomena that occur in a variety of materials and geometries. The method is implemented in a feedback-controlled sputtering system that provides fine control over ion beam exposure and sample temperature. We call the method "ion-beam sculpting", and apply it to the problem of fabricating a molecular-scale hole, or nanopore, in a thin insulating solid-state membrane. Such pores can serve to localize molecular-scale electrical junctions and switches[4–6] and function as masks[7] to create other small-scale structures. Nanopores also function as membrane channels in all living systems, where they serve as extremely sensitive electromechanical devices that regulate electric potential, ionic flow, and molecular transport across cellular membranes[8]. We show that ion-beam sculpting can be used to fashion an analogous solid-state device: a robust electronic detector consisting of a single nanopore in a Si_3N_4 membrane, capable of registering single DNA molecules in aqueous solution.

When massive ions with energies of several thousand electron-volts impinge on a surface, an atomic-scale erosion process, called sputtering, removes approximately one atom from the surface for every incident ion[9–12]. We reasoned that as material is removed from a flat Si_3N_4 surface containing a cavity on its opposite surface (Fig. 1a, top), the flat surface will ultimately intercept the bottom of the bowl shaped cavity, forming a nanopore (Fig. 1a, bottom). Creating a molecular-scale pore requires knowing precisely when to stop the erosion process. The apparatus illustrated in Fig. 1b implements a feedback-controlled ion sputtering system that counts the ions transmitted through the opening pore and extinguishes the erosion process at the appropriate time. The apparatus also controls a number of parameters that we discovered to be important to the ion-beam sculpting process. These include: (1) sample temperature; (2) ion beam duty cycle (defined as the time the beam was on, divided by the sum of the times it was on and off, for pulsed beams); and (3) the instantaneous ion beam flux, F, in ions $nm^{-2}\,s^{-1}$ when the beam is on the sample.

A sample with a large (~0.1-μm diameter) bowl-shaped cavity was fabricated in a free-standing Si_3N_4 membrane supported on a silicon frame (Fig. 1a). To create a molecular-scale nanopore, the sample was ion-sculpted using 3-keV Ar^+ ions in the apparatus described above. Surprisingly, experiments on this sample at room temperature did not yield the expected result; a nanopore did not open even after excessively long ion beam exposure. We discovered why by ion-sculpting a membrane that contained a through-hole, rather than a bowl-shaped cavity. At room temperature, the transmitted ion counting rate clearly decreased with increasing ion beam exposure (Fig. 2a), suggesting that the hole was closing rather than opening. The incident beam was switched off when the counting rate fell to 40 counts s^{-1} (Fig. 2a, inset). Transmission electron microscope (TEM) images of the hole before and after the ion-beam exposure (Fig. 2b and c) revealed that the hole size had indeed

been reduced from 60 nm to 1.8 nm by the growth of a thin membrane (of the order of 10 nm, as deduced from electron microscopy). With sufficient ion beam exposure the nanopore completely closed, and the ion count fell to zero. Thus, in addition to ion-sputter erosion, there must be a lateral atomic flow of matter into the pore, stimulated by the ion beam. That this is a surface, or near-surface, phenomenon is strongly suggested by computer simulations that show the ion beam energy to be deposited within less than 5 nm of the sample surface (J. F. Ziegler and J. P. Biersack, SRIM-2000, available at http://www.research.ibm. com/ion/ionbeams).

The flow of matter to the developing nanopore is temperature-dependent (Fig. 3). A transition between pore opening and pore closing was consistently seen at about 5 °C under the ion-beam conditions of Fig. 3. When pore area is plotted versus dose rather than time (Fig. 4), the slope of the data reveals that for continuous beam exposure (grey trace, Fig. 4) the efficiency of pore closing per incident ion is clearly greater at low fluxes than at high fluxes. Figure 4 also shows that a pulsed beam (black data points) closes pores more efficiently than does a continuous ion beam at the same instantaneous flux.

Our demonstrated ability to monitor changing dimensions continuously in the nanometre range while varying experimental parameters provides an unusual opportunity to test microscopic models to account for the observed materials phenomena. Competing processes are probably at work. One is responsible for opening the pore, probably driven by ion-sputter erosion of the pore edge. This process is probably dominant at low temperatures and high fluxes. Established sputtering phenomenology[9] could account for this process, although a full understanding will depend on knowing the detailed geometrical shape of the pore, not just its diameter.

Two different views can explain the motion of matter necessary to account for the pore-closing phenomenon. First, a very thin (~5 nm) stressed viscous surface layer may be created by the energy and matter deposited by the ion beam. An enhanced collective motion, driven by a reduced viscosity and/or enhanced stress owing to implantation effects or surface tension, causes the layer to relax. A similar model has been invoked for atomic transport in sputter-induced rippling (refs 13–15).

Second, we can account for our observations with a model in which incident ions both create and annihilate excess, independent and mobile surface 'adatoms' (for example, atoms or molecular clusters) that can diffuse to the pore. Adatom diffusion has been successfully invoked in modelling sputter-induced ripple formation on Si(001)[16,17].

We propose that the concentration of surface adatoms $C(\mathbf{r}, t)$, is governed by a two-dimensional diffusion equation:

$$\frac{\partial}{\partial t}C(\mathbf{r},t) = FY_{\mathrm{a}} - FC\sigma - \frac{C}{\tau_{\mathrm{trap}}} + D\boldsymbol{\nabla}^2 C \qquad (1)$$

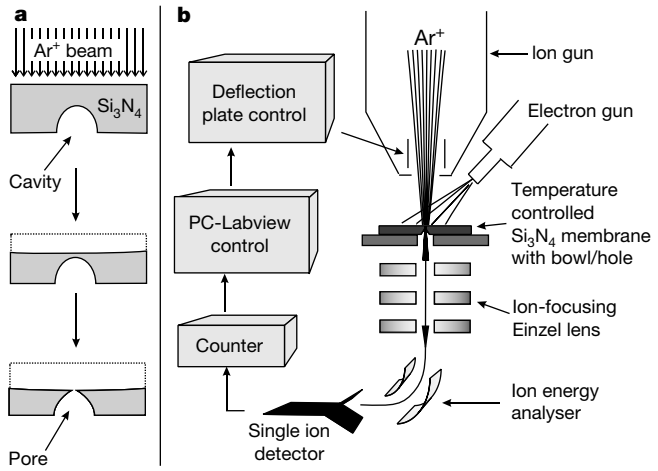

Figure 1 Strategy to make nanopores using argon ion-beam sputtering. **a**, Sputtering removes material from a free-standing Si_3N_4 membrane with a cavity. **b**, Feedback-controlled ion-beam sculpting apparatus housed in a high-vacuum chamber. **a**, A 500-nm-thick low-stress (~200 MPa tensile) Si_3N_4 film was deposited on a (100) silicon substrate by low-pressure chemical vapour deposition[25]. Photolithography and directional wet chemical etching of silicon were used to create a free-standing 25 μm × 25 μm Si_3N_4 membrane[26]. Either a bowl-shaped cavity (**a**), or a single initial pore of ~0.1 μm diameter (not shown), was created near the centre of the membrane using, respectively, reactive ion etching[27] or a focused ion beam (FIB) machine[26]. **b**, A differentially pumped ion gun (VG Microtech model EX05) exposes the sample surface to an Ar^+ beam, ~0.2 mm in diameter. A Channeltron (Gallileo Optics) electron-multiplier-style single-ion detector, positioned after the sample, counts transmitted ions. Deflection plates at the exit port of the ion gun could deflect the beam off the sample or pulse the ion beam on and off the sample. A focusing Einzel lens and 60° electrostatic deflection system between sample and detector are used to suppress electron, ion and X-ray backgrounds. A 50-eV electron gun (Kimball Physics Model FRA-2x1-1) floods the sample to neutralize surface charging. A liquid-nitrogen-cooled shroud surrounds the sample and Einzel lens and a quadrupole mass spectrometer, connected to the 10^{-9} torr turbo-pumped vacuum chamber, monitors residual gas composition. A thermocouple monitors the sample holder temperature, which is adjusted with cold nitrogen gas and a resistance heater.

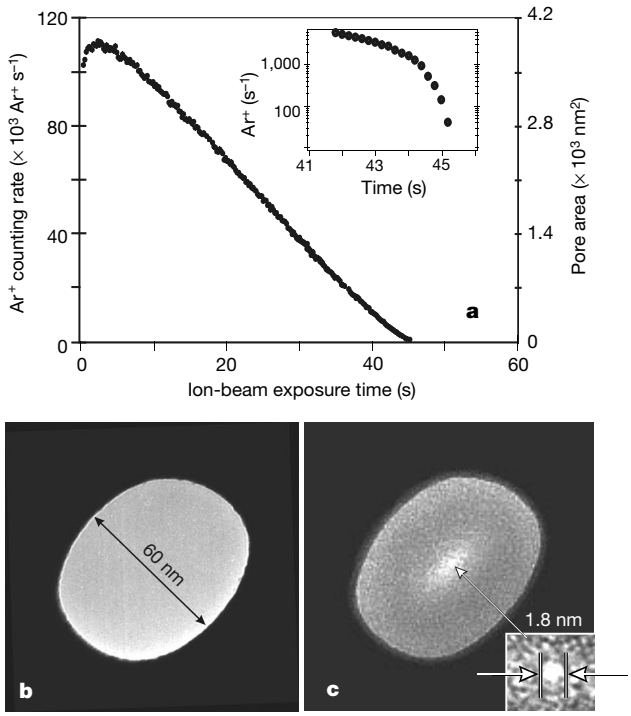

Figure 2 Sculpting a nanopore. **a**, Transmitted ion count rate (left axis) and pore area (right axis) versus integrated time the ion beam is on the 28 °C sample. **b**, TEM image of initial 61-nm diameter pore made by FIB in a 500-nm Si_3N_4 membrane. **c**, TEM image of the same sample after Ar^+ ion-beam exposure. Energy-dispersive analysis of X-rays in the TEM reveals the presence of Si and N in the membrane that has filled the pore, although the precise composition has not been quantified. Because the transmitted ion current is directly proportional to the area of the pore, the instantaneous pore area indicated in all figures was calculated by multiplying the initial pore area (determined by TEM) by the ratio of the instantaneous to initial transmitted ion current. Temperature, 28 °C. Flux, 28 $Ar^+ s^{-1} nm^{-2}$. Duty cycle, 200 ms/1 s.

where **r** and t are surface position and time. D is the adatom surface-diffusion coefficient and F the incident ion-beam flux. $\partial C/\partial t$ depends on: (1) a generation rate, taken proportional to the incoming flux through Y_a; (2) an annihilation rate proportional to F and C through an annihilation cross-section σ, and an annihilation rate due to trapping at surface defects, assumed to be proportional to C through τ_{trap}^{-1}, with τ_{trap} a lifetime. Term (2) causes the model to exhibit a reduced efficiency of pore closing per incident ion at increased fluxes.

The pore boundary is taken to be a perfect sink for adatoms, which are there transformed to a thin layer of accumulating matter that accounts for pore closure. (A vacancy source at the pore, instead, could also produce this effect.) Our boundary condition could arise from capillary forces, which under equilibrium conditions drive the pore to close when the radius of curvature in the plane of the membrane is smaller than that in an axial section, and vice versa. The pore size at which the actual transition between opening and closing occurs could be altered by the influence of ion bombardment on the energetics or kinetics governing atomic transport.

From steady-state solutions to equation (1) the diffusional flux into the pore can be obtained. There results a characteristic distance from the pore edge, X_m, within which adatoms are more likely to reach the pore than be annihilated by traps or ion erosion, where:

$$\frac{1}{X_m^2} = \frac{1}{D\tau_{trap}} + \frac{\sigma}{D}F \qquad (2)$$

Adatoms beyond X_m are more likely to be annihilated before they reach the pore.

In low-temperature experiments, where diffusional contributions to pore closure are presumably frozen out (see Fig. 3), the sputter-erosion process that contributes to pore opening can be determined. We include this process (assumed to be temperature-independent) taking $Y_a \approx 1$ and a pore thickness of about 10 nm, and fit X_m for each incident flux at 28 °C (where pores close); this yields the solid curves in Fig. 4. As expected, X_m increases with decreasing flux, which accounts for the enhanced pore-closing efficiency at low flux. The resulting X_m values are consistent with equation (2), as shown in the inset of Fig. 4, from which $D \approx 10^3$ nm^2 s^{-1} is extracted from a linear fit using $\sigma \approx 0.1$ nm^2 as a reasonable estimate.

The model qualitatively explains the pulsed ion-beam observations. When the ion beam is off, adatoms remain on the surface, but the adatom annihilation channel associated with the incident beam flux disappears. Thus, after the beam is extinguished, the remaining adatoms may diffuse to the pore periphery from greatly increased X_m. This can significantly increase the efficiency per ion for pore closing. The enhanced pore closing with increasing temperature can be accounted for by a thermally activated adatom diffusion coefficient.

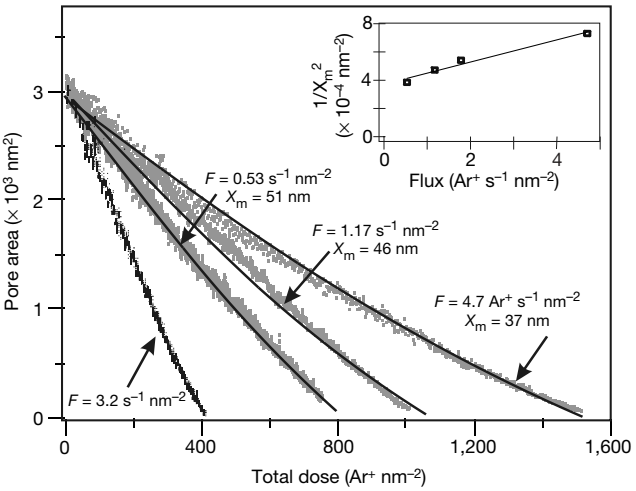

Figure 4 Flux dependence of ion-beam sculpting. Pore area versus total dose for samples exposed at different instantaneous fluxes, F, to a continuous beam (grey traces), or a pulsed beam (black traces). Duty cycle, 100 ms/1 s. The plotted black curves overlying the grey data points are predicted from the diffusion model under steady-state conditions (see text). The inset plots $1/X_m^2$ versus flux, from which D is extracted. Temperature, 28 °C.

The diffusion model presented above is phenomenological and contains idealizations and assumptions connected with our ignorance of many microscopic properties of matter under ion beam exposure. Nevertheless, extensions of the studies demonstrated here, using pulsed as well as continuous beam exposures at different temperatures, should permit the determination of materials-specific parameters like D, τ_{trap}, Y_a and σ that will enable fabrication of useful nanoscale devices.

To demonstrate such a device we sculpted a nanopore in a Si_3N_4 membrane for use as a single-molecule electronic detector of DNA. Proteinaceous nanopores, or channels, have been inserted into lipid bilayers in aqueous solutions where they serve as electronic sensors to identify and characterize single molecules[18–20]. But proteins in lipid bilayers are labile and the channel diameters they provide cannot easily be adjusted. Robust, solid-state nanopores, fashioned to any desired diameter, could yield new data and understanding of transport in confined spaces, and will make it possible to create robust single-molecule-sensing devices to characterize molecules of

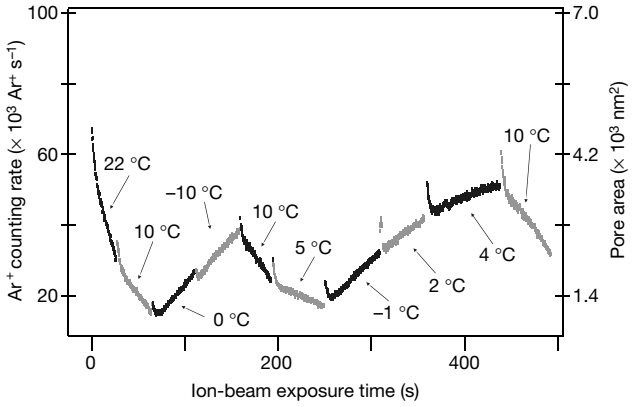

Figure 3 Temperature dependence of ion-beam sculpting. Successive data sets at different temperatures (shown) are delimited by their alternate black and grey coloration. Flux, 14 Ar$^+$ s^{-1} nm^{-2}. Duty cycle, 200 ms/1 s.

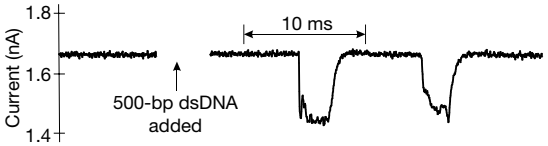

Figure 5 Molecular events in a nanopore detector. A Si_3N_4 membrane with a 5-nm pore separated two compartments filled with saline solution (1 M KCl, 10 mM Tris-HCl, 1 mM EDTA, pH 8.0). Initially, with only the saline solution in the compartments, a 120-mV bias between AgCl electrodes in each compartment resulted in a constant ionic current of 1.66 nA through the nanopore. This was consistent with the known conductivity of the ionic solution, assuming a pore length of around 10 nm. After adding double-stranded DNA, 500 base pairs long, to the negatively biased compartment, and allowing time for diffusion, intermittent current blockades (two are illustrated) were observed. Si_3N_4 membranes with holes of about 100 nm in diameter that were completely closed by ion-beam sculpting produced 20 GΩ seals.

DNA and other biopolymers at unprecedented speeds. Using electrophysiology techniques[8,21], we tested one of our robust, electrically quiet, 5-nm-diameter pores with double-stranded DNA. After applying a voltage bias that would draw the negatively charged DNA molecules through the nanopore, we observed diminutions of the ionic current (Fig. 5), reminiscent of the ionic-current blockages observed when single strands of DNA are translocated through the channel formed by α-haemolysin in a lipid bilayer[22,23]. Because no such blockages were seen during one hour of monitoring before adding DNA, and because the blockages ceased when the voltage bias was reversed, we attribute these blockages to interactions of individual DNA molecules with the nanopore. The duration of these blockades was on the order of milliseconds, and they consistently exhibited current reductions to 88% of the open-pore value. This last value is commensurate with translocation of a rod-like molecule whose cross-sectional area is 3–4 nm^2 (ref. 24).

The experimental observations, model considerations and the demonstration of an electronic device show that ion-beam sculpting represents a promising new approach to nanoscale fabrication. With feedback control, reproducibility does not depend on precisely matching all conditions and starting dimensions. The method should be useful for fabricating a variety of nanoscale semiconductor devices, as similar sculpting phenomena have been observed for geometries such as thin slits, trenches and crosses, in several materials, like SiO_2, Si and Al. Furthermore, next-generation ion-source arrays and mask technologies (see http://www-afrd.lbl.gov/ ibt.html) combined with multichannel ion detectors will allow highly parallel applications of nanoscale ion sculpting methods. □

Received 6 February; accepted 11 May 2001.

1. Ito, T. & Okazaki, S. Pushing the limits of lithography. *Nature* **406,** 1027–1031 (2000).
2. Joachim, C., Gimzewski, J. K. & Aviram, A. Electronics using hybrid-molecular and mono-molecular devices. *Nature* **408,** 541–548 (2000).
3. Stupp, S. I. & Braun, P. V. Molecular manipulation of microstructures: Biomaterials, ceramics, and semiconductors. *Science* **277,** 1242–1248 (1997).
4. Reed, M. A., Zhou, C., Deshpande, M. R. & Muller, C. J. The electrical measurement of molecular junctions. *Ann. NY Acad. Sci.* **852,** 133–144 (1998).
5. Zhou, C., Deshpande, M. R. & Reed, M. A. Nanoscale metal/self-assembled monolayer/metal heterostructures. *Appl. Phys. Lett.* **71,** 611–613 (1997).
6. Ralph, D. C., Black, C. T. & Tinkham, M. Spectroscopic measurements of discrete electronic states in single metal particles. *Phys. Rev. Lett.* **74,** 3241–3244 (1995).
7. Deshmukh, M. M., Ralph, D. C., Thomas, M. & Silcox, J. Nanofabrication using a stencil mask. *Appl. Phys. Lett.* **75,** 1631–1633 (1999).
8. Hille, B. *Ionic Channels and Excitable Membranes* (Sinauer, Sunderland, Massachusetts, 1992).
9. Johnson, R. E. & Shou, J. Sputtering of inorganic insulators. *K. Danske Vidensk. Selsk. Mat.-fys. Meddr.* **43,** 403–494 (1993).
10. Sigmund, P. Introduction to sputtering. *K. Danske Vidensk. Selsk. Mat.-fys. Meddr.* **43,** 7–26 (1993).
11. Nenandovic, T., Perraillon, B., Bogdanov, Z., Djordjevic, Z. & Milic, M. Sputtering and surface topography of oxides. *Nucl. Instrum. Methods B* **48,** 538–543 (1990).
12. Gnaser, H. *Ion Irradiation of Solid Surfaces* (Springer, Berlin/Heidelberg, New York, 1999).
13. Mayer, T. M., Chason, E. & Howard, A. J. Roughening instability and ion-induced viscous relaxation of SiO_2 surfaces. *J. Appl. Phys.* **76,** 1633–1643 (1994).
14. Carter, G. Viscoelastic buckling and plastic-flow deterministic mechanistic mechanisms for ripple initiation on ion bombarded amorphous solids. *Surf. Interf. Anal.* **25,** 952–954 (1997).
15. Brongersma, M. L., Snoeks, E., Dillen, T. V. & Polman, A. Origin of MeV ion irradiation-induced stress changes in SiO_2. *J. Appl. Phys.* **88,** 59–64 (2000).
16. Erlebacher, J., Aziz, M. J., Chason, E., Sinclair, M. B. & Floro, J. A. Spontaneous pattern formation on ion bombarded Si(001). *Phys. Rev. Lett.* **82,** 2330–2333 (1999).
17. Erlebacher, J., Aziz, M. J., Chason, E. & Aziz, M. J. Nonlinear amplitude evolution during spontaneous patterning of ion-bombarded Si(001). *J. Vacuum Sci. Technol. A* **18,** 115–120 (2000).
18. Kasianowicz, J., Brandin, E., Branton, D. & Deamer, D. W. Characterization of individual polynucleotide molecules using a membrane channel. *Proc. Natl Acad. Sci. USA* **93,** 13770–13773 (1996).
19. Bezrukov, S. M., Vodyanoy, I. & Parsegian, V. A. Counting polymers moving through a single ion channel. *Nature* **370,** 279–281 (1994).
20. Gu, L. Q., Braha, O., Conlan, S., Cheley, S. & Bayley, H. Stochastic sensing of organic analytes by a pore-forming protein containing a molecular adaptor. *Nature* **398,** 686–690 (1999).
21. Hammill, O. P., Marty, A., Neher, E., Sakmann, B. & Sigworth, F. J. Improved patch-clamp techniques for high-resolution current recording from cells and cell-free membrane patches. *Eur. J. Physiol.* **391,** 85–100 (1981).
22. Akeson, M., Branton, D., Kasianowicz, J. J., Brandin, E. & Deamer, D. W. Microsecond time-scale discrimination among polycytidylic acid, polyadenylic acid, and polyuridylic acid as homopolymers or as segments within single RNA molecules. *Biophys. J.* **77,** 3227–3233 (1999).
23. Meller, A., Nivon, L., Brandin, E., Golovchenko, J. & Branton, D. Rapid nanopore discrimination between single polynucleotide molecules. *Proc. Natl Acad. Sci. USA* **97,** 1079–1084 (2000).
24. Bezrukov, S. M. Ion channels as molecular coulter counters to probe metabolite transport. *J. Membr. Biol.* **174,** 1–13 (2000).
25. Wolf, S. & Tauber, R. N. *Silicon Processing for the VLSI Era* 149–224 (Lattice, Sunset Beach, California, 2000).
26. Rai-Choudhury, P. (ed.) *Handbook of Microlithography, Micromachining, and Microfabrication* 41–97, 153–195 (SPIE-International Society for Optical Engineering, Bellingham, Washington, 1997).
27. Ralls, K. S., Buhrman, R. A. & Tiberio, R. C. Fabrication of thin-film metal nanobridges. *Appl. Phys. Lett.* **55,** 2459–2461 (1989).

Acknowledgements

This work was supported by the US Defense Advanced Research Projects Agency, the National Science Foundation and the US Department of Energy.

Correspondence and requests for materials should be addressed to J.A.G. (e-mail: golovchenko@physics.harvard.edu).

Ordered nanoporous arrays of carbon supporting high dispersions of platinum nanoparticles

Sang Hoon Joo*, Seong Jae Choi*, Ilwhan Oh†, Juhyoun Kwak†, Zheng Liu‡, Osamu Terasaki‡§ & Ryong Ryoo*

* *National Creative Research Initiative Center for Functional Nanomaterials and Department of Chemistry, Korea Advanced Institute of Science and Technology, Taejon 305-701, Korea*
† *Electrochemistry Laboratory, Department of Chemistry, Korea Advanced Institute of Science and Technology, Taejon 305-701, Korea*
‡ *CREST, Japan Science and Technology Corporation, Department of Physics, Tohoku University, Sendai 980-8578, Japan*
§ *Department of Physics and Center for Interdisciplinary Research, Tohoku University, Sendai 980-8578, Japan*

Nanostructured carbon materials are potentially of great technological interest for the development of electronic[1,2], catalytic[3,4] and hydrogen-storage systems[5,6]. Here we describe a general strategy for the synthesis of highly ordered, rigid arrays of nanoporous carbon having uniform but tunable diameters (typically 6 nanometres inside and 9 nanometres outside). These structures are formed by using ordered mesoporous silicas as templates, the removal of which leaves a partially ordered graphitic framework. The resulting material supports a high dispersion of platinum nanoparticles, exceeding that of other common microporous carbon materials (such as carbon black, charcoal and activated carbon fibres). The platinum cluster diameter can be controlled to below 3 nanometres, and the high dispersion of these metal clusters gives rise to promising electrocatalytic activity for oxygen reduction, which could prove to be practically relevant for fuel-cell technologies. These nanomaterials can also be prepared in the form of free-standing films by using ordered silica films as the templates.

Various production methods[7] such as arc discharge, laser ablation, chemical vapour deposition, and template synthesis techniques[8] are used to obtain carbon nanotubes in the single-wall, multi-wall or disordered-wall form. In general, during synthesis of the nanotubes, the tube diameters are very difficult to control. The carbon nanotubes are obtained as a powder, with separate or entangled nanotubes that exhibit a broad distribution in tube diameters. Some of the single-wall nanotubes undergo self-organization to a bundle[9]. However, the organization is achieved through weak van der Waals interactions, so that the bundle cannot be considered as a system with rigid structural periodicity. Here we